Fiber optic pressure sensor with self-compensation capability for harsh environment applications

Hai Xiao
Jiangdong Deng, MEMBER SPIE
Zhiyong Wang
Wei Huo
Po Zhang
Ming Luo
Gary R. Pickrell, MEMBER SPIE
Russell G. May, MEMBER SPIE
Anbo Wang
Virginia Polytechnic Institute and State University
Bradley Department of Electrical and Computer Engineering
Center for Photonics Technology
Blacksburg, Virginia 24061

Abstract. A novel fiber optic pressure sensor system with self-compensation capability for harsh environment applications is reported. The system compensates for the fluctuation of source power and the variation of fiber losses by self-referencing the two channel outputs of a fiber optic extrinsic Fabry-Pérot interfrometric (EFPI) sensor probe. A novel sensor fabrication system based on the controlled thermal bonding method is also described. For the first time, high-performance fiber optic EFPI sensor probes can be fabricated in a controlled fashion with excellent mechanical strength and temperature stability to survive and operate in the high-pressure and high-temperature coexisting harsh environment. Using a single-mode fiber sensor probe and the prototype signal-processing unit, we demonstrate pressure measurement up to 8400 psi and achieved resolution of 0.005% (2σ=0.4 psi) at atmospheric pressure, repeatability of ±0.15% (±13 psi), and 25-h stability of 0.09% (7 psi). The system also shows excellent remote operation capability when tested by separating the sensor probe from its signal-processing unit at a distance of 6.4 km.
[DOI: 10.1117/1.1917570]

Subject terms: fiber optic sensors; Fabry-Perot; interferometers.

Paper 040283 received May 17, 2004; revised manuscript received Nov. 27, 2004; accepted for publication Dec. 1, 2004; published online May 4, 2005.

1 Introduction

Accurate pressure measurement in harsh environment is essential in many industrial processes. For example, pressure information of the underground oil reservoir is one of the most commonly used parameters to determine the quantity of the oil reserve and to optimize the operation of oil extraction.[1–3] In many applications, conventional pressure sensors are often found to have difficulty withstanding severe environmental conditions. This situation has opened a new but challenge opportunity for the sensor society to provide robust, high-performance, and cost-effective pressure sensors capable of operating in various harsh environments.

Optical-fiber-based sensors have many advantages over conventional electronic sensors for harsh environment applications. These include small size, lightweight, immunity to electromagnetic interference, resistance to chemical corrosion, avoidance of ground loops, high sensitivity, huge bandwidth, capability of remote operation, and ease of integration into large-scale fiber networking and communication systems.[4] These advantages have promoted a worldwide research activity in optical fiber sensors for harsh environment applications.[4,5] Optical fiber pressure sensors have been demonstrated based on various mechanisms including microbending,[6] photoelastics,[7–9] and fiber gratings sensors.[10–12]

Optical fiber extrinsic Fabry-Pérot interferometers (EFPIs) have been developed into pressure sensors.[13–16] Compared to fiber optic Mach-Zehnder and Michelson interferometric sensors,[17,18] the EFPI sensor has the advantages of smaller size and the immunity to the polarization fading. Moreover, because the reference and signal waves are packed very closely together, there is a potential advantage to minimize the temperature dependence of the sensor.

The simplest signal-processing method for the EFPI sensors is direct interference fringe counting, which has been the dominant signal-processing method in early EFPI sensors. However, if the measurement range exceeds half of the interference fringe, due to the nonlinear and periodic nature of the sinusoidal interference fringes, the fringe-counting method suffers from problems such as sensitivity reduction and fringe direction ambiguity when the sensor reaches peaks or valleys of the interference fringe. Proposed by Murphy et al., it was possible to count fringes bidirectionally using a quadrature-phase-shifted two-interferometer structure.[19] However, it was found difficult to maintain the exact phase difference between these two interferometers in practical applications.

More recently, several signal-processing methods that have been developed for other types of fiber interferometers were reported being used in EFPI sensors. Steward et al.[20] reported their research on applying laser wavelength-modulation-based heterodyne interferometry to demodulate the interference signal of EFPI sensors. White light scanning interferometry has also been used for EFPI sensors.[21,22] These systems used a second interferometer with its optical path difference scanned to match the optical path difference of the EFPI sensor. Lo and Sirkis[23] and Schmidt and Furstenau[24] reported using multiple wavelengths to interrogate the EFPI cavity length. The dynamic

0091-3286/2005/$22.00 © 2005 SPIE

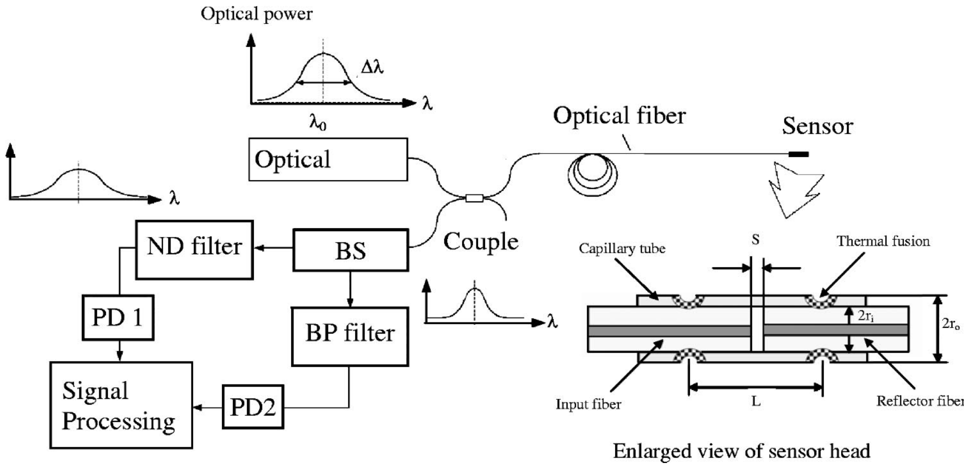

Fig. 1 Illustration of the principle of fiber optic sensor system: PD, photodetector; BP filter, bandpass filter; ND filter, neutral density filter; BS, beamsplitter.

range of the measurement was increased because the effective wavelength of this technique became the beat wavelength of the multiple sources, which was much larger than that of a single source. However, the stability of the sensor was a concern because the wavelengths of the multiple sources could drift in different directions.

Fiber EFPI sensors have been commonly fabricated by inserting two endface-cleaved fibers into a capillary tube with a proper inner diameter.[25] Epoxies have been used to bond the fibers to the capillary tube. Although extensive research has been conducted to find high-performance epoxies to fabricate EFPI sensor probes, the fabricated sensors generally failed to provide satisfactory performance in terms of mechanical strength and thermal stability. Another constraint of the epoxy-based sensors is that the maximum operating temperature is limited by that of the epoxy, which is relatively low. Because epoxies have a coefficient of thermal expansion (CTE) inherently different from that of the fibers and the tube, epoxy-bonded sensors are usually very sensitive to temperature changes, which makes it difficult to use those sensors to measure parameters other than temperature. It is also found difficult to control the sensor initial cavity length and the bonding size due to the relatively long curing time of the epoxy. Furthermore, the viscosity of the epoxy bonding will also degrade the frequency response of the EFPI sensor in the case where high-frequency signals must be measured.

In summary, although optical-fiber-based pressure sensors have the potential opportunity to replace the majority of conventional electronic pressure transducers in existence in today's sensor market, technical difficulties still exist and delay this becoming a reality. The most common concerns of fiber optic pressure sensors include the stability issue and the cross-sensitivity among multiple environmental parameters. The fluctuation of source power and the change in fiber loss can easily introduce errors to the measurement results, which make most optical-fiber-based sensors unstable. Although the source power fluctuation can be compensated by monitoring a portion of the light split from the source at the input to the fiber, this compensation does not include the loss fluctuation of the fiber path from the source to the sensor probe and back to the signal-processing unit. In practical applications, the fiber link from the source to the sensor may be long and subject to environment-dependent loss variations. Therefore, a complete compensation requires not only covering the source power fluctuation but also the fiber losses. The fact that most fiber sensors are cross-sensitive to temperature also makes it difficult to use fiber optic sensors to measure parameters other than temperature in many practical applications.

In this paper, we present a fiber optic EFPI pressure sensor with self-compensation capability for harsh environment applications. The system compensates for the fluctuation of source power and the variation of fiber losses by self-referencing the two channel outputs of a fiber optic EFPI sensor probe. Because the two channel signals are derived from the same optical source and propagate the same length of fiber, the source power fluctuation and the fiber loss variations can be completely compensated by taking the ratio of these two signals. The sensor probe is designed and fabricated to operate within a portion of the half interference fringe so that the ambiguity of direction in traditional fringe counting can be circumvented.

2 Principle of Operation

2.1 *System Configuration*

The basic configuration of the fiber sensor system can be illustrated using Fig. 1. The system includes a sensor probe, a broadband source, an optoelectronic signal-processing unit, and optical fibers linking the sensor probe and the signal-processing unit.

The light from the broadband optical source (e.g., an LED) is launched into a 50% fiber coupler through the pigtailed fiber, and propagates along the optical fiber to the sensor head. The sensor head is constructed by inserting two optical fibers, with their endfaces cleaved, into a capillary tube so that an air-gaped low-finesse Fabry-Pérot cavity is formed between the two fiber endfaces, as shown in the enlarged view of the sensor head. The incident light is first partially reflected ($\sim$4%) at the endface of the input fiber. The remainder of the light propagates across the air gap to the endface of the reflector fiber, where a second reflection ($\sim$4%) is generated. The two reflections then travel back along the same fiber and through the same fiber coupler to the signal-processing unit. The signal processing unit of the sensor system extracts the information of the Fabry-Pérot cavity length, which is related to various measurands governed by the corresponding physical laws.

2.2 *Signal Processing*

As shown in Fig. 1, the reflected light from the sensor head is split into two channels by a polarization insensitive beamsplitter (BS). Channel 2 passes an optical bandpass (BP) filter with its center wavelength aligned with the center wavelength of the broadband source. Channel 1 passes through a neutral density (ND) filter so that the light intensity at photodetector 1 (PD1) is balanced to that at photodetector 2 (PD2). The light in channel 1 remains its original spectral width (broadband spectrum), while the light in channel 2 has a narrower spectrum because the spectrum width of the optical BP filter is narrower than the source spectrum.

Because of the low reflectance of the fiber endfaces, the interference signals resulting from the two channels can be approximated by two-beam interferometry. Assume I_{s_1,s_2} are the spectral power densities of the two channels, respectively, and take an infinitesimal section of the spectrum with a spectrum width of dλ, the interference signals of the two chennels resulted from this small spectrum are given by[26]

$$\mathrm{d}I_{1,2}=RI_{s_1,s_2}\,\mathrm{d}\lambda+R(1-R)I_{s_1,s_2}\,\mathrm{d}\lambda+2\{(RI_{s_1,s_2}\,\mathrm{d}\lambda)[R(1-R)I_{s_1,s_2}\,\mathrm{d}\lambda]\}^{1/2}\times\cos\left(\frac{4\pi}{\lambda}L+\phi_0\right), \tag{1}$$

where R is the reflectance at the boundary of the air and the fiber endface, L is the cavity length, and ϕ_0 is the initial phase difference of the two light waves.

The interference signals of the two channels are therefore the result of integration of Eq. (1) over their entire spectra, which is given by

$$I_{1,2}=\int_{-\infty}^{\infty}\left[2RI_{s_1,s_2}-R^2I_{s_1,s_2}+2R(1-R)^{1/2}I_{s_1,s_2}\cos\left(\frac{4\pi}{\lambda}L+\phi_0\right)\right]\mathrm{d}\lambda. \tag{2}$$

The reflectance at the fiber endfaces is approximately 4% of the total incident optical power. Because the reflectance is relatively small, the interference signals given by Eq. (2) can thus be further approximated by

$$I_{1,2}\approx 2R\int_0^{\infty}I_{s_1,s_2}(\lambda)\left[1-\cos\left(\frac{4\pi}{\lambda}L+\phi_0\right)\right]\mathrm{d}\lambda. \tag{3}$$

In principle, continuously tracking the phase change of the interference fringes of the two channels would measure the sensor cavity change in length. However, the fiber loss variations and the source power drift could introduce errors to the amplitude of the interference signal and result in a poor accuracy of the measurement. To avoid these two adverse effects, we introduce the output from channel 1 to the signal processing as a reference signal, and the sensor system output is evaluated as the ratio of the two signals of the two channels, given by

$$s=\frac{I_2}{I_1}=\frac{\int_{-\infty}^{\infty}I_{s_2}(\lambda)\{1+\cos[(4\pi/\lambda)L+\phi_0]\}\mathrm{d}\lambda}{\int_{-\infty}^{\infty}I_{s_1}(\lambda)\{1-\cos[(4\pi/\lambda)L+\phi_0]\}\mathrm{d}\lambda}. \tag{4}$$

From the theories of optics, we know that the coherence length of a source is inversely proportional to its spectral width. If the optical path difference (OPD) of the interferometer is larger than half the coherence length of the source being used, the two optical waves will not effectively interfere to generate interference fringes. As mentioned, the two channels have different spectral widths because of the use of the optical bandpass filter in channel 2. They thus have different coherence lengths.

Figure 2(a) shows the calculated interference signals of the two channels as a function of the cavity length based on Eq. (3), where the interference signal strengths have been normalized with respect to their total powers, and the source is assumed to be an LED. The center wavelength of the LED is 1310 nm and the spectral width is 70 nm. The optical bandpass filter has a center wavelength of 1310 nm and a spectral width of 10 nm. The source spectrum and the transmission spectrum of the optical bandpass filter are illustrated in Fig. 2(b).

If we fabricate the sensor probe in such a way that it has an initial cavity length that is larger than the coherence length of channel 1 but smaller than the coherence length of channel 2, then, as shown in Fig. 2(a), channel 1 becomes the noninterference channel with its intensity relatively unchanged as $I_1=2RI_{10}$, where I_{10} is the average power of channel 1. Channel 2 remains its highly visible interference fringes as the cavity length changes, which can be further simplified to

$$I_2=2RI_{20}\left[1+\gamma\cos\left(\frac{4\pi}{\lambda}L+\phi_0\right)\right], \tag{5}$$

where I_{20} is the average optical power of channel 2; $\overline{\lambda}$ is the mean wavelength of channel 2; and γ is the fringe visibility of the interference signal, which is defined by

$$\gamma=\frac{I_{2,\max}-I_{2,\min}}{I_{2,\max}+I_{2,\min}}, \tag{6}$$

where $I_{2\max}$ and $I_{2\min}$ are the maximum and minimum powers of the optical interference signal, respectively. The fringe visibility in our case is a function of R and L, and most importantly the spectral width of the light source.

When the cavity length is longer than half the coherence length of channel 1 but shorter than that of channel 2, the ratio of the two channel's signals becomes

$$s=\frac{I_2}{I_1}\approx\alpha\left[1+\gamma\cos\left(\frac{4\pi}{\lambda}L+\phi_0\right)\right], \tag{7}$$

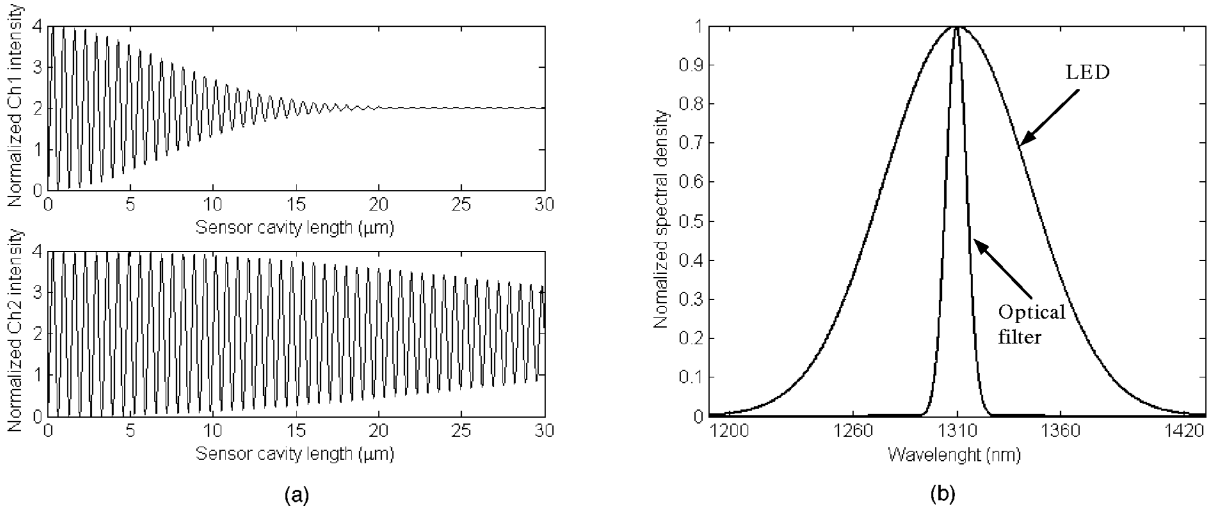

Fig. 2 (a) Interference signals as a function of the sensor cavity length and (b) the source spectrum (spectral width, 70 nm) and the transmission spectrum of the optical bandpass filer (spectral width, 10 nm).

where $\alpha = I_{20}/I_{10}$ is the ratio of the average optical powers of the two channels. Figure 3(a) plots the ratio given by Eq. (7) as the function of the sensor cavity length. Because the two channel signals are from the same source and experience the same transmission paths, they record the same information of source power fluctuation and fiber loss variations. The α in Eq. (7) becomes a constant. The ratio of the outputs from channel 2 and channel 1 is only a function of the Fabry-Pérot cavity length (L). The two sources of errors can thus be eliminated from the final result of measurement. Because channel 2 uses a narrow bandpass filter to slice a small portion of the spectrum of the broadband source, I_{20} is significantly smaller than I_{10}. To minimize the division error, the optical powers of the two channels are balanced roughly by inserting a neutral density filter in channel 1 before PD1, as shown in Fig. 1. The small residual power imbalance is further balanced by adjusting the gains of the electric amplifiers of the two channels.

If we design and fabricate the sensor probe to operate only over the semi-linear range of a half fringe, as shown in Fig. 3(b), a one-to-one quantitative relation between the output intensity and the sensor cavity length is obtained. Note that both the increasing side and decreasing side of an interference fringe can be used for measurement. When exposed to an external pressure, the sensor cavity length changes correspondingly. After a calibration process that correlates the sensor cavity length change to known pressures, the output intensity can thus be used to measure the applied pressure.

3 Sensor Probe Design

The geometry of the fiber optic pressure sensor probe is illustrated in the enlarged view of sensor head, as shown in Fig. 1. When a hydrostatic pressure is applied, the capillary tube will deform, and as a consequence the cavity length will change. By monitoring the sensor cavity length change, the applied pressure can thus be measured. The

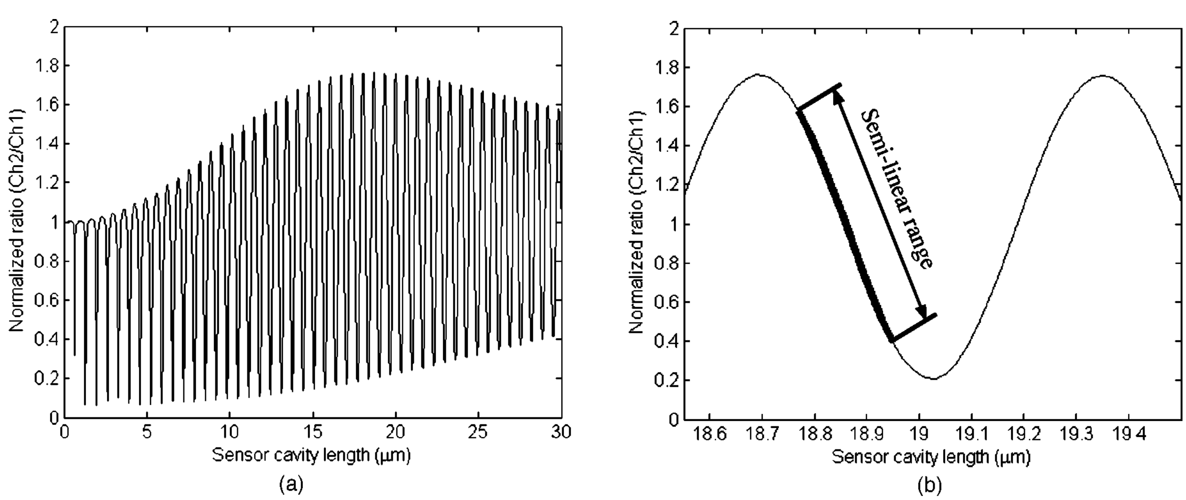

Fig. 3 (a) Ratio of the two-channel signals and (b) illustration of the semilinear operating range of the interference fringe.

sensor probe is designed to be immersed in hydraulic fluid in actual applications, for example, in underground oil reservoir, effects in both the longitudinal and the transverse directions should be considered in modeling its pressure response.

If we assume that the capillary tube has an outer radius of r_o and an inner radius of r_i, the sensor cavity length change (ΔL) resulting from the applied pressure p can be expressed as[27,28]

$$\Delta L = \frac{L}{E}[\sigma_z - \mu(\sigma_r - \sigma_t)], \tag{8}$$

where L is the effective sensor gauge length defined as the distance between the two thermal bonding points, E is the Young's modulus, and μ is the Poisson's ratio of the capillary tube. For fused silica glasses, $E = 74\,\mathrm{GPa}$ and $\mu = 0.17$.

In Eq. (8), three pressure-induced stresses have been considered: σ_r is the radial stress, σ_t is the tangential stress, and σ_z is the longitudinal stress. These three stresses can be calculated by the following equations:

$$\sigma_r = \frac{r_o^2}{r_o^2 - r_i^2}\left(1 - \frac{r_i^2}{r_o^2}\right)(p - p_0), \tag{9}$$

$$\sigma_t = \frac{r_o^2}{r_o^2 - r_i^2}\left(1 + \frac{r_i^2}{r_o^2}\right)(p - p_0), \tag{10}$$

$$\sigma_z = \frac{r_o^2}{r_o^2 - r_i^2}(p - p_0), \tag{11}$$

where p is the applied pressure, and p_0 is the internal pressure inside the cavity.

Combining Eqs. (8) through (11), the cavity length change ΔL can be related to the applied pressure p by

$$\Delta L = \frac{L r_o^2}{E(r_o^2 - r_i^2)}(1 - 2\mu)(p - p_0). \tag{12}$$

Equation (12) indicates that the change of the sensor cavity length is proportional to the difference of the applied pressure (p) and the internal pressure (p_0). Therefore, the sensor can be directly used as a differential pressure gauge. If the initial sensor cavity length is calibrated to a known pressure, we can use the sensor to measure the absolute pressure by monitoring the change of the cavity length.

Temperature cross-sensitivity is a concern for any pressure sensor. In the EFPI structure, the temperature effect is partially compensated because the capillary tube expands to enlarge the gap while the fibers expand to reduce the gap when temperature increases. However, this is true to some extent. The residual temperature effects can be attributed to the difference between the thermal expansion coefficients (TECs) of the fiber and the tube, and the thermal expansion of the uncompensated gap portion (L). As the gauge length reduces to achieve a large dynamic range, the temperature effect becomes worse. A detailed investigation of the temperature cross-sensitivity of the fiber pressure sensor will be reported in a separate paper.

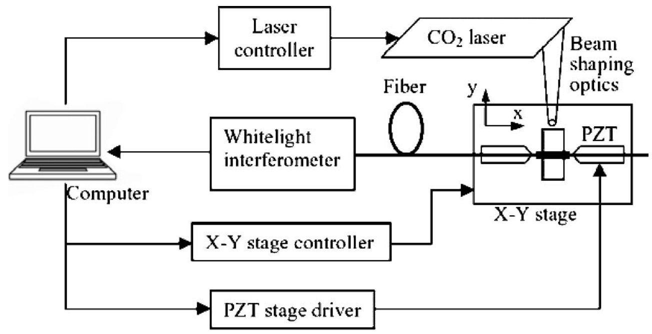

Fig. 4 Schematic of the automated sensor fabrication system.

4 Sensor Probe Fabrication

4.1 *Controlled Thermal Bonding*

To survive a high-pressure and high-temperature coexisting harsh environment, fiber sensor probes must be fabricated with good mechanical strength and high thermal stability. In addition to survivability, the sensor probe also must deliver demanding performance. The bonding should not have adverse effects on the optical properties of the fiber waveguide. The initial cavity length of the sensor probe must be accurately adjusted to a certain optimal value so that the signal channel can produce interference fringes with good fringe visibility while the reference channel excludes any interference effect. The initial sensor operating point also must be precisely adjusted to the starting point of the semilinear portion of the interference fringe. This enables the operating range of the sensor to cover the full semilinear portion of the interference fringe. The sensor effective gauge length (the distance between the two bonding points) must be controlled within a tight tolerance so that the fabricated sensors have predictable and repeatable performances. The fabrication of the sensor should be automatic or semiautomatic so that the sensor can be made in a large quantity with good repeatability and at a low cost.

The key challenge is then to permanently bond the capillary tube and the fibers together in a controlled fashion. Apparently a conventional epoxy-based sensor structure is not a valid solution. Telecommunication optical fibers are made by doping very small amount of germanium into pure silica glass. Silica glass is an amorphous material. By locally heating the fiber and tube assembly to a temperature above which the glass is softened, the silica tube and the optical fiber can flow into each other and locally join to form a solid bond.

4.2 *System Configuration*

An automated sensor fabrication system was developed based on the controlled thermal bonding technique. As shown in Fig. 4, the automated sensor probe fabrication system includes three subsystems. They are the high-energy carbon dioxide (CO_2) laser, providing the heating power to thermally fuse the optical fiber and the capillary tube together; the computer-controlled micromotion stage system

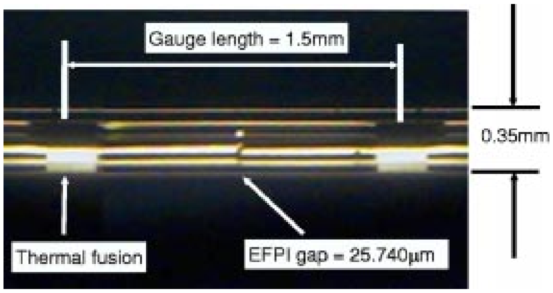

Fig. 5 Microscopic photograph of the sensor probe (gauge length, 1.5 mm; initial cavity length, 25.740 μm).

to enable real-time accurate adjustment of the sensor cavity length and the effective gauge length; and the fiber optic white light spectrum interferometry signal-processing unit to monitor the cavity length of the sensor in real-time during fabrication. A personal computer is used to coordinate these three subsystems so that the CO_2 laser output power, the motion of the stages, and the sensor cavity lengths can be precisely controlled during the sensor fabrication process.

The CO_2 laser used in the system is a SYNRAD, Inc., Model 48-2. The wavelength emitted by the laser is 10.6 μm, and the maximum output power under continuous mode operation is 25 W. When the silica glass material is exposed to the laser beam, it absorbs the optical energy and converts it to thermal energy, which enables the silica glass materials to be heated locally up to very high temperatures. Through a specially designed interface, the output power and the duration of the laser output can be precisely controlled to generate an optimal heating trajectory, which normally includes a preheating section, a thermal fusion section, and an annealing section.

The white light fiber interferometric subsystem provides real time measurement of the sensor cavity length during the fabrication process. Illuminating the sensor probe with a broad-spectrum source, the sensor cavity length is measured by demodulating the interference spectrum of the sensor probe.[29] A computer program was developed to demodulate the interference spectral signals so that the cavity length of the sensor can be monitored accurately while the sensor is fabricated. The standard deviation of the white light subsystem was measured to be σ=0.001 μm.

During the sensor fabrication, the fibers and the capillary tube must be kept precisely aligned. The bonding distance, which determines the sensor effective gauge length, also needs to be precisely controlled. Several ultraprecise micropositioning stages are used to enable precisely moving the two fibers in three dimensions. The sensor cavity length can thus be accurately adjusted to the preset value.

Figure 5 shows a microscopic photograph of a typical sensor probe. We can clearly see the sensor cavity formed by the fiber endfaces and the two fusion points. The shortest sensor gauge length that can be fabricated with the system is about 0.5 mm. It is very difficult to further reduce the sensor gauge length because the fiber endfaces can be damaged, resulting from the too-close fusion point.

5 System Design and Implementation

A prototype sensor system was designed to operate at the center wavelength of 1310 nm and to use single-mode fiber to transmit optical signals between the sensor probe and the signal-processing unit. The source used for the single-mode fiber-based system is a high-power superluminescent light-emitting diode (SLED) provided by Anritsu Corp. (AS3B281FX), with a center wavelength of 1310 nm, a spectral width of 40 nm, and an output power of 1.21 mW from a 9/125-μm pigtailed single-mode fiber.

A polarization-insensitive BS with a splitting ratio of 50:50 at the wavelength of 1310 nm was used to split the light signal from the sensor head into two channels. At one channel, the light passed an optical ND filter and was detected by a large-effective-area InGaAs PD and amplified to offer the reference signal. The light in the other channel passed through an optical BP filter with its center wavelength at 1310 nm and an FWHM spectral width of 10 nm. Because the spectral width of this channel is much narrower than that of the other channel, an interferometric signal can thus be obtained after the photodetection.

The signal-processing requires a ratio function to compensate for the unwanted optical power fluctuation. The ratio of the two channels is performed digitally through the host computer. A 23-bit data acquisition system purchased from Lawson Labs Inc. was used in the system to convert the analog output from the two channels to digital data. Computer programs were written to interface the analog-to-digital (A/D) system so that two channels were sampled alternatively. A finite impulse response (FIR) filter was designed in the software to further filter the high-frequency noise. After the dark current correction, the ratio of the two channels data was mapped to pressure output through the prestored calibration curve.

6 Experiments and Results

6.1 *Pressure Sensor Calibration*

Before the sensor system can be used for actual pressure measurement, it must be calibrated to relate the output ratio to the applied pressure. The sensor calibration is conducted by applying known pressures to the sensor within the semi-linear operating range. The one-to-one relation between the sensor output and the applied pressure forms the calibration curve, which can be stored in the host computer and later used to convert the sensor output to the pressure reading.

The sensor calibration system was constructed based on a computer-controlled high-performance pressure generator/controller manufactured by Advanced Pressure Products, Inc. The system configuration is shown in Fig. 6. The pressure controller/generator can supply a hydrostatic pressure up to 20,000 psi, and the accuracy of the pressure output is 0.1% of the full scale.

During the calibration process, the pressure sensor was installed inside the pressure calibration chamber. The hydrostatic pressure was applied to the sensor at the increment of 1/40 of the estimated linear range of the pressure sensor. The built-in pressure gauge of the calibration system measured the hydrostatic pressure inside the chamber and the system saved the data as applied pressures. At the same time, the output of the sensor system was sampled through the A/D converter and stored as another data file.

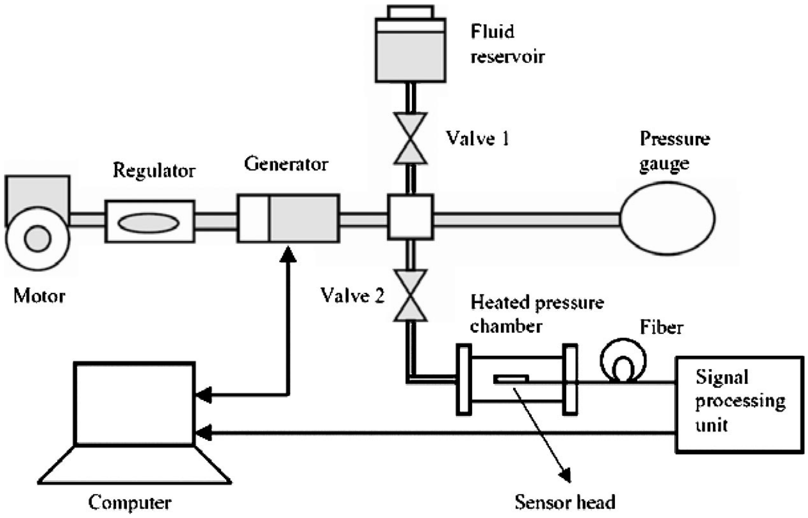

Fig. 6 Block diagram of pressure sensor calibration/evaluation system.

To ensure the accuracy of the calibration, the system held the pressure at each step for about 50 s before moving to the next step. By taking the average within the pressure-holding period, the error was minimized. The one-to-one relation of the applied pressure and the sensor output was then used to find the calibration equation through polynomial fitting. Usually, the calibration curve was obtained by taking the average of several consecutive calibration data to further ensure the accuracy of calibration. Figure 7 plots the sensor outputs versus the applied pressures resulting from the calibration process. The sensor used in the test was a single-mode fiber sensor with the gauge length of 0.5 mm, an initial cavity length of 25.46 μm, and an interference fringe visibility of 70%.

6.2 *Resolution*

The resolution of the sensor system can be interpreted by its standard deviation of pressure measurements. It is common to use twice the standard deviation as the direct measure of resolution. The evaluation of the sensor resolution was performed using a calibrated sensor with the linear range of 8400 psi. The sensor was exposed to the atmosphere where the pressure reading from the sensor should be zero. The data from the sensor system was sampled at a rate of 10 samples/s for 3 min. The pressure measurement outputs within the 3-min sampling period are plotted in Fig. 8. The standard deviation of the pressure data within this time period was calculated to be σ=0.2 psi. Therefore the resolution of the sensor system was estimated to be 2σ=0.4 psi. The normalized resolution with respect to the dynamic range (8400 psi) of the system was 0.005% of the full scale.

Note that the resolution of the sensor is not constant within the entire operating range due to the nonlinear nature of the interference signal. The test data at atmospheric pressure only gives an estimate. The evaluation of the system resolution at other pressures becomes difficult because of the instability of the pressure calibration system.

6.3 *Repeatability*

The repeatability of the sensor system was measured by applying pressure to a certain preset point repeatedly from one direction (increasing or decreasing). The largest difference of the sensor output readings were used to specify the repeatability of the sensor. The calibrated single-mode sen-

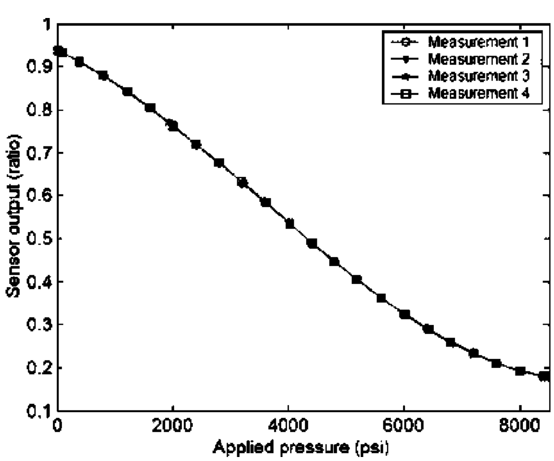

Fig. 7 Pressure sensor response to applied calibration pressures.

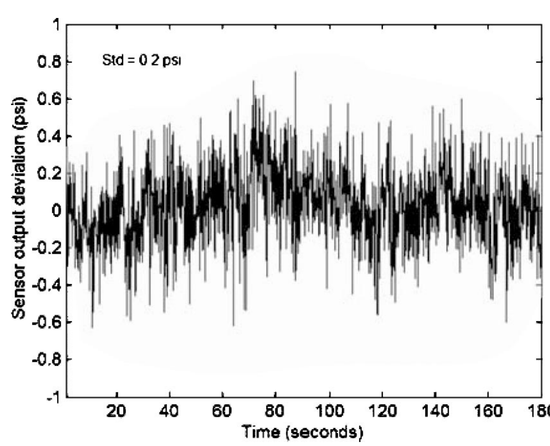

Fig. 8 Standard deviation of pressure measurement under atmospheric pressure.

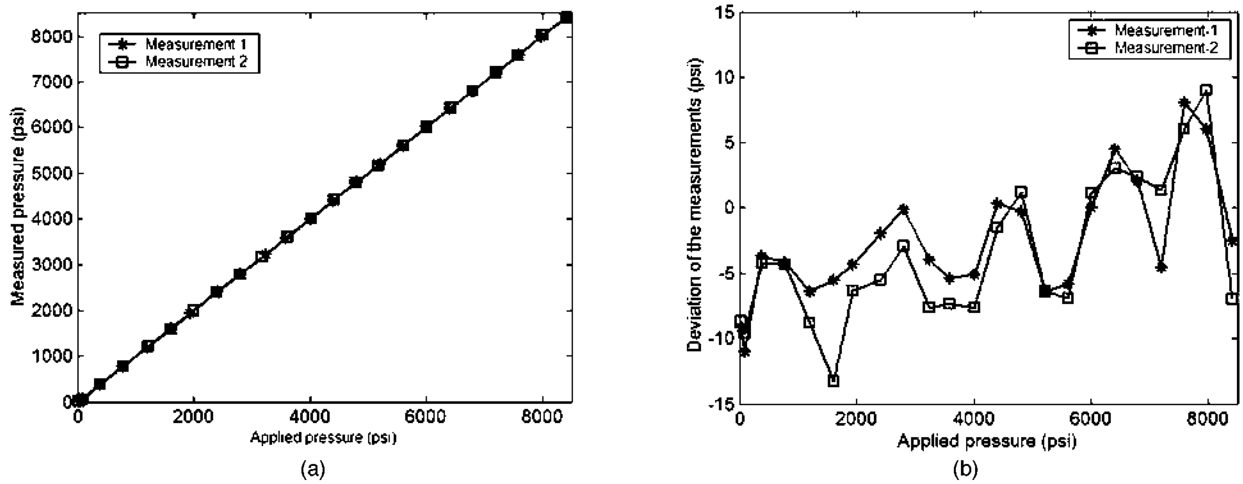

Fig. 9 (a) Repeatability test of the pressure measurement and (b) deviation of the test results.

sor was used to evaluate the repeatability of the system. Two consecutive measurements up to the full operating range of the sensor were performed with the results shown in Fig. 9(a). The deviation of the two measurement results with respect to the calibration data are plotted in Fig. 9(b).

The maximum deviation between the measured pressure and the calibrated pressure was within ± 13 psi. The normalized repeatability of the sensor system with respect to its dynamic range (8400 psi) was therefore $\pm 0.15\%$ of the full scale.

6.4 *Stability*

The same single-mode sensor with the operating range of 8400 psi was also used to test the system stability. The sensor was kept in the pressure test chamber of the APP hydrostatic pressure calibration system for 25 h starting from 4:00 p.m. in the afternoon. The pressure of the chamber was maintained to the atmospheric pressure. The data acquisition system was programmed to sample the sensor's output every 10 s. The test result is shown in Fig. 10. The maximum peak-to-peak pressure variation within the 25-h time period was about 7 psi. The normalized maximum variation was thus about 0.09% of the full dynamic range of 8400 psi.

6.5 *Pressure Measurement Over a Distance*

One of the advantages of using a fiber optic sensor is its capability of remote operation. The pressure sensor probe can be deployed to the remote site at a distance that is far away from its signal-processing unit. Pressure signals can be transmitted from the sensor probe back to the signal-processing unit through an optical fiber. Although the optical fiber attenuates the signal strength, and in real applications, the fiber attenuation might even vary as the environmental parameters change, the designed pressure sensor system can compensate for the change of the fiber loss by self-referencing one channel's signal to the other.

To test the remote operation capability of the single-mode fiber pressure sensor system, we separated the sensor probe from its signal-processing unit by inserting a spool of optical fiber (SMF28™ by Corning Inc.). The length of the optical fiber was 6.4 km. With a typical loss of 0.3 dB/km at 1310 nm, the total round-trip loss of the signal was about 4 dB. The pressure measurement results are plotted in Fig. 11(a), and the deviations of the measured pressures and the applied pressures are shown in Fig. 11(b). The sensor system provided a reliable pressure measurement up to its designed dynamic range of 8400 psi, of course, with a minor degradation of accuracy from ± 13 to ± 28 psi.

7 Conclusions

A novel fiber optic pressure sensor with self-compensation capabilities was developed to provide robust and reliable pressure measurement in a harsh environment. The sensor system compensates for source power fluctuations and fiber loss variations by self-referencing its two channel outputs. The sensor achieves high resolution with very simple signal processing by confining the operating range of the sensor within the semilinear portion of the half interference fringe, which also circumvents the phase ambiguity problem.

A novel sensor fabrication system based on the controlled thermal bonding method was developed. The sensor fabrication system uses a CO_2 laser to thermally fuse the capillary tube and fiber together. The sensor fabrication system provides real-time control and accurate adjustment of

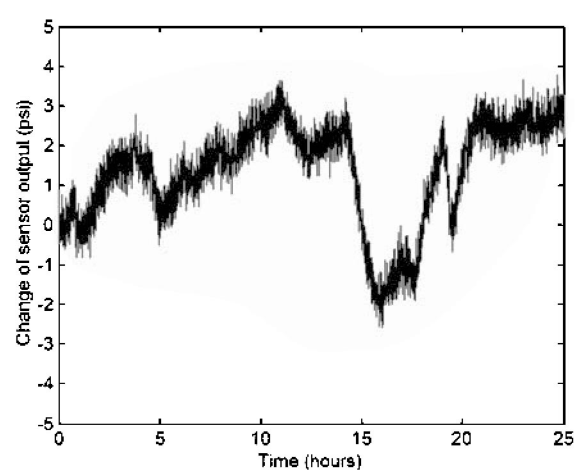

Fig. 10 System stability test results for the period of 25 h.

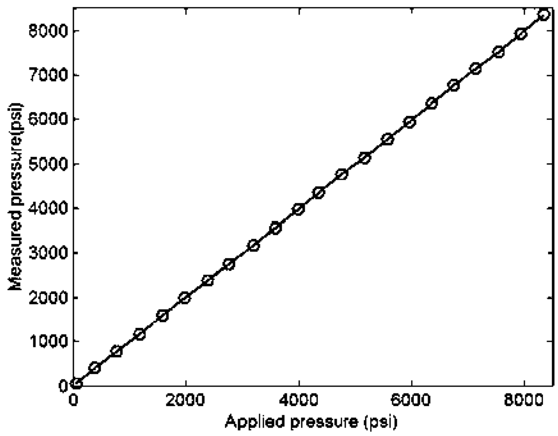

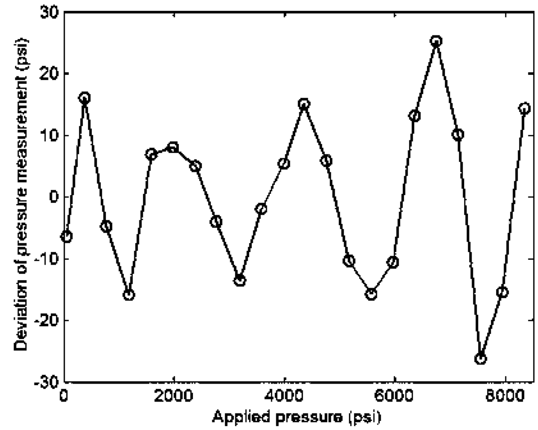

Fig. 11 (a) Remote pressure measurement and (b) deviation of pressure measurement performed at a distance of 6.4 km.

the sensor cavity length and gauge length. For the first time, high-performance fiber optic Fabry-Pérot sensor probes can be fabricated in a controlled fashion with excellent mechanical strength and temperature stability that enhance the sensor's capability of operating in harsh environments.

Using a single-mode fiber sensor probe with a dynamic range of 8400 psi, the performance of the pressure sensor system was studied systematically. The system achieved resolution of 0.005% ($2\sigma=0.4$ psi) at atmospheric pressure, repeatability of $\pm 0.15\%$ (± 13 psi), and 25-h stability of 0.09% (7 psi). Separating the sensor probe from its signal-processing unit at a distance of 6.4 km, the sensor system was also tested to show an excellent remote operation capability.

Acknowledgments

The research work was jointly sponsored by the National Petroleum Technology Office (NPTO) under the Department of Energy (DOE) and Chevron Research Company.

References

1. R. J. Schroeder, R. T. Romos, and T. Yamate, "Fiber optic sensors for oilfield services," *Proc. SPIE* **3860**, 12–22 (1999).
2. A. Mendez, R. Dalziel, and N. Douglas, "Applications of optical fiber sensors in subsea and downhole oil well environment," *Proc. SPIE* **3860**, 23–34 (1999).
3. A. D. Kersey and F. K. Didden, "CiDRA: leveraging multi-channel telecommunications technology for enhanced downhole monitoring capabilities in the oil & gas industry," *Proc. SPIE* **3860**, 35–41 (1999).
4. E. Udd, *Fiber Optic Sensors: An Introduction for Engineers and Scientists*, Wiley, New York (1991).
5. B. Culshaw, W. C. Michie, and P. T. Gardiner, "Smart structures-the role of fiber optics," *Proc. SPIE* **2341**, 134–151 (1994).
6. J. W. Berthold, "Historical review of microbend fiber-optic sensors," *J. Lightwave Technol.* **13**(7), 1193–1199 (1995).
7. W. B. Spillman, "Multimode fiber-optic pressure sensor based on the photoelastic effect," *Opt. Lett.* **7**(8), (1982).
8. I. P. Giles, S. McNeill, and B. Culshaw, "A stable remote intensity based fiber sensor," *J. Phys.* **18**, 1124–1126 (1985).
9. A. Wang, S. He, X. Fang, X. Jin, and J. Lin, "Optical fiber pressure sensor based on photoelastic effect and its applications," *J. Lightwave Technol.* **10**(10), 1466–1472 (1992).
10. D. J. Hill and G. A. Cranch, "Gain in hydrostatic pressure sensitivity of coated fiber Bragg grating," *Electron. Lett.* **35**(15), 1268–1269 (1999).
11. M. G. Xu, H. Geiger, and J. P. Dakin, "Fiber grating pressure sensor with enhanced sensitivity using a glass-bubble housing," *Electron. Lett.* **32**(2), 128–129 (1996).
12. U. Sennhauser, A. Frank, P. Mauron, and P. M. Nellen, "Reliability of optical fiber Bragg grating sensors at elevated temperature," in *Proc. 38th Annu. 2000 IEEE Int. Symp. on Reliability Physics*, pp. 264–269 (2000).
13. Y. J. Rao and D. A. Jackson, "Prototype fiber optic based pressure probe with bilt-in temperature compensation with signal recovery by coherence reading," *Appl. Opt.* **32**(34), (1993).
14. A. Wang, H. Xiao, J. Wang, Z. Wang, W. Zhao, and R. G. May, "Self-calibrated interferometric-intensity-based optical fiber sensors," *J. Lightwave Technol.* **19**(10), (2001).
15. M. A. Chan, S. D. Collins, and R. L. Smith, "A micromachined pressure sensor with fiber optic interferometric readout," *Sens. Actuators* **43**(1–3), 196–201 (1994).
16. Y. Kim and D. P. Neikirk, "Micromachined Fabry-Perot cavity pressure transducer," *IEEE Photonics Technol. Lett.* **7**(12), (1995).
17. A. Dandridge, "Acoustic sensor development at NRL," in *Proc. Acoustic Society of America Annual Meeting*, Miami, FL (1987).
18. A. Dandridge and A. D. Kersey, "Overview of mach-Zehnder sensor technology and applications," in *Fiber Optic and Laser Sensors VI, Proc. SPIE* **985**, (1988).
19. K. A. Murphy, M. F. Gunther, A. M. Vengsarkar, and R. O. Claus, "Quadrature phase shifted extrinsic Fabry-Perot fiber optic sensors," *Opt. Lett.* **16**(4), 273–275 (1991).
20. G. Stewart, A. Mencaglia, W. Philp, and W. Jin, "Interferometric signals in fiber optic methane sensors with wavelength modulation of the DFB laser source," *J. Lightwave Technol.* **16**(1), 43–53 (1998).
21. C. Chang and J. Sirkis, "Absolute phase measurement in extrinsic Fabry-Perot optical fiber sensors using multiple path-match conditions," *Exp. Mech.* **37**(1), 26–32 (1996).
22. G. Zuliani, W. D. Hogg, K. Liu, D. Janzen, and R. M. Measures, "Demodulation of a fiber Fabry-Perot strain sensor using white light interferometry," *Proc. SPIE* **1588**, 308–313 (1991).
23. Y. Lo and J. S. Sirkis, "Fabry-Perot sensors for dynamic studies using spectrally based passive quadrature signal processing," *Exp. Mech.* **37**(2), 119–125 (1997).
24. N. Schmidt and M. Furstenau, "Fiber optic extrinsic Fabry-Perot interferometric sensors with three wavelength digital phase demodulation," *Opt. Lett.* **24**(9), 599–601 (1999).
25. K. A. Murphy, M. F. Gunther, R. G. May, R. O. Claus, T. A. Tran, J. A. Greene, and P. G. Duncan, "EFPI sensor manufacturing and applications," *Proc. SPIE* **2721**, 476–482 (1996).
26. P. Hariharan, *Optical Interferometry*, 2nd ed., p. 151, Academic Press (2003).
27. B. B. Muvdi and J. W. McNabb, *Engineering Mechanics Materials*, pp. 597–602, Macmillian, New York (1984).
28. E. J. Hearn, *Mechanics of Materials*, pp. 194–217, Pergamon Press (1977).
29. H. Xiao, J. D. Deng, G. R. Pickrell, R. G. May, and A. Wang, "Single crystal sapphire fiber-based strain sensor for high temperature applications," *J. Lightwave Technol.* **21**(10), 2276–2283 (2003).

Hai Xiao received BS and MS degrees in precision instrument and optoelectronics engineering from Tianjin University, China, in 1991 and 1993, respectively, and a PhD degree in electrical engineering from Virginia Polytechnic Institute and State University (Virginia Tech), Blacksburg, in 2000. From 1998 to 2000, he was a senior research associate at the Center for Photonics Technologies, where he worked on optical fiber sensors, biomedical optics, optical fiber communication devices, and three-dimensional imaging systems. From 2000 to 2003, he was a member of the technical staff at the Optoelectronic Center of Lucent Technologies (now Agere Systems), Breinigsville, Pennsylvania, working on optical fiber amplifiers, photonic devices, and subsystems. He is currently an assistant professor in the Electrical Engineering Department of the New Mexico Institute of Mining and Technology, Socorro, New Mexico. His research interests include photonic sensors and networks, optical communications, and computer visions. Dr. Xiao is a senior member of IEEE, and a member of OSA, SPIE, and LEOS.

Jiangdong Deng received a PhD in electrical engineering from Virginia Polytechnic Institute and State University in 2005. He also received PhD, MS, and BS degrees in condensed matter physics from Nankai University, China. From 2001 to 2004, he worked at NanoOpto Corporation, Somerset, New Jersey, as a senior engineer. In 2004, he joined the Center for Imaging and Masoscale Structure of Harvard University, as a principal technologist/researcher. His research interests have included nanophysics, nanostructure-based devices, nanofrabrication technology, optical fiber sensors, optical fiber communication devices, nondestructive optical detection for microdefects, and crystal growth. Dr. Deng is a member of the Optical Society of America (OSA), Institute of Electrical and Electronics Engineers (IEEE), and the International Society for Optical Engineers (SPIE).

Zhiyong Wang received his master's degree from the Department of Electrical and Computer Engineering of Virginia Tech and joined the Optical Fiber Research Department of Bell Laboratories (Lucent Technologies) as a fiber optic engineer in 2000. He continued to work in the same department, which became the central research arm of OFS-Fitel LLC. He joined the Department of Electrical and Computer Engineering at Virginia Tech to pursue a PhD in 2002. He has published 24 referred scientific conference and journal papers, and holds one patent disclosure. His research interests involve long-period fiber gratings, self-assembled nanomaterials, and fiber optic sensors.

Wei Huo: Biography and photograph not available.

Po Zhang received the BS degree in radio propagation from the Department of Space Physics, Wuhan University, and the MS degree in inorganic nonmetallic materials from Shanghai Institution of Optics and Fine Machinery, Academia Science of China, Shanghai, in 1984 and 1990, respectively. He obtained a PhD degree in electrical Engineering from Virginia Polytechnic Institute and State University (Virginia Tech) in 2003. From 1994 to 1999, he was a senior engineering researcher in the National Key Fiber Optical R&D Center, where his research scope covered fiber optical sensors, gyroscopes system, photonics components, and fiber optical applications. At Virginia Tech, he worked on optical fiber sensors for harsh environments, fiber Bragg grating sensor systems, and high-density multiplexing technology. Currently, he has been working on biomedical applications and chemical sensors based on state-of-the-art photonics technology as a postdoctoral associate in the Department of Physics and Astronomy of Michigan State University since 2004.

Ming Luo received BS, MS, and PhD degrees in precision instrument and optoelectronics engineering from Tianjin University, China, in 1991, 1994, and 1996, respectively. She also received an MS degree in electrical engineering from Virginia Polytechnic Institute and State University (Virginia Tech), Blacksburg, Virginia, in 2000. From 2000 to 2002, she was a member of the technical staff at the Optoelectronic Center of Lucent Technologies (now Agere Systems), Breinigsville, Pennsylvania, working on the industry's first large-scale all-optical switch product based on micro-electro-mechanical systems (MEMS), MEMS equalization filters, and add-drop prototypes and subsystems. She is currently an electrical research engineer at the Petroleum Recovery Research Center of the New Mexico Institute of Mining and Technology, Socorro, New Mexico. Her research interests include photonic sensors, control software, and computer vision.

Gary R. Pickrell received BS and MS degrees in ceramic engineering from Ohio State University in 1985 and 1987, respectively, and a PhD in materials engineering science from Virginia Tech in 1994. He is an assistant professor in the Materials Science and Engineering Department and associate director of the Center for Photonics Technology in the Electrical and Computer Engineering Department at Virginia Tech. His industrial experience includes various research, development and technical management positions at Owens Illinois, Corning, Selee, and Porvair Advanced Materials. He has authored over 70 technical papers, is an R&D 10 award winner, is a member of the editorial board of the *International Journal of Six Sigma* and on the international editorial board of the *Sensors* journal, and has 9 patents issued as well as 6 additional patents pending. His current research is focused on random hole optical fibers and optical fiber sensors, glass, ceramic, and various other aspects of materials science and engineering, and business improvement methodologies including Six Sigma and Lean Six Sigma.

Russell G. May: Biography and photograph not available.

Anbo Wang: Biography and photograph not available.